Optics and Lasers in Engineering 174 (2024) 107937

Contents lists available at ScienceDirect

Optics and Lasers in Engineering

journal homepage: www.elsevier.com/locate/optlaseng

Semi-heuristic phase compensation in digital holographic microscopy for stable and accurate quantitative phase imaging of moving objects

Sofía Obando-Vásquez [a], Ana Doblas [b], Carlos Trujillo [a,*]

[a] Applied Optics Group, School of Applied Science and Engineering, Universidad EAFIT, Medellín, Colombia
[b] Department of Electrical and Computer Engineering, University of Massachusetts Dartmouth, New Bedford, MA 02747, USA

ARTICLE INFO

Keywords:
Hologram video reconstruction
Digital holographic microscopy
Off-axis phase compensation
Telecentric configuration
Quantitative phase imaging
Semi-heuristic algorithm
Phase background stability

ABSTRACT

Digital holographic microscopy (DHM) is a cutting-edge interferometric technique to recover the complex wavefield scattered by microscopic samples from digitally recorded intensity patterns. In off-axis DHM, the challenge is digitally generating the reference wavefront replica to compensate for the tilt between the interfering waves. Current methods to estimate the reference wavefront's parameters rely on brute-force grid searches or heuristics algorithms. Whereas brute-forced searches are time-consuming and impractical for video-rate quantitative phase imaging and analysis, applying heuristics methods in holographic videos is limited since the phase background level occasionally changes between frames. A semi-heuristic phase compensation (SHPC) algorithm is proposed to address these challenges to reconstruct phase images with minimum distortion in the full field-of-view (FOV) from holograms recorded by a telecentric off-axis digital holographic microscope. The method is tested with a USAF test target, smearing red blood cells and alive human sperm. The SHPC method provides accurate phase maps as the reference brute-force method but with a 92-fold reduction in processing time. Furthermore, this method was tested for reconstructing experimental holographic videos of dynamic specimens, obtaining stable phase values and minimal differences in the background between frames. This proposed method provides state-of-the-art phase reconstructions with high accuracy and stability in holographic videos, allowing the successful XYZ tracking of single-moving sperm cells.

1. Introduction

Digital holographic microscopy (DHM) is a non-invasive imaging technique that recovers the complex wavefield scattered by microscopic samples using a digital sensor without staining or fixation procedures [1,2]. DHM has been extensively utilized across various scientific fields, including microelectromechanical systems evaluation [3,4], monitoring and observation of cells and particles within a specific volume [5–9], and the characterization of cellular responses to environmental changes, such as the presence of pathogens or drugs [10,11]. The last two applications involve dynamic biological processes that require accurate, stable, and rapid phase map reconstruction algorithms.

Off-axis DHM systems enable fast and accurate quantitative phase imaging in a single shot. However, these systems require a tilting angle between the interfering wavefronts to separate the spectrum of the desired object information from the unwanted twin image and DC term in the Fourier domain [12]. In 2000, Cuche et al. proposed a Fourier filtering mask to select the spatial frequencies of the object and reconstruct the complex amplitude distribution [13]. However, the center and dimension of the filter mask must be chosen precisely to avoid imprecise phase measurements. Off-axis image-plane DHM systems operating in the telecentric regime [14] are considered the most straightforward DHM systems as they involve minimal numerical processes [15]. Firstly, selecting the spatial object frequencies in the spectrum of the DHM hologram, and, secondly, the compensation of the tilting angle between interfering waves. Incorrectly selecting the object frequencies can result in amplitude and phase measurements with low resolution. On the other hand, inaccurate compensation for the tilting angle can introduce errors in the reconstructed quantitative phase measurements [14]. One straightforward method for compensating and achieving precise phase extraction involves manually determining the tilting angle until a phase reconstruction without sawtooth fringes is obtained. However, choosing the best-reconstructed phase image can be challenging for DHM end-users since it heavily depends on their expertise. Any DHM reconstruction algorithm should be automatic (i.e., without user intervention) and provide accurate phase measurements

* Corresponding author.
E-mail address: catrujilla@eafit.edu.co (C. Trujillo).

https://doi.org/10.1016/j.optlaseng.2023.107937
Received 3 October 2023; Received in revised form 31 October 2023; Accepted 7 November 2023
Available online 16 November 2023

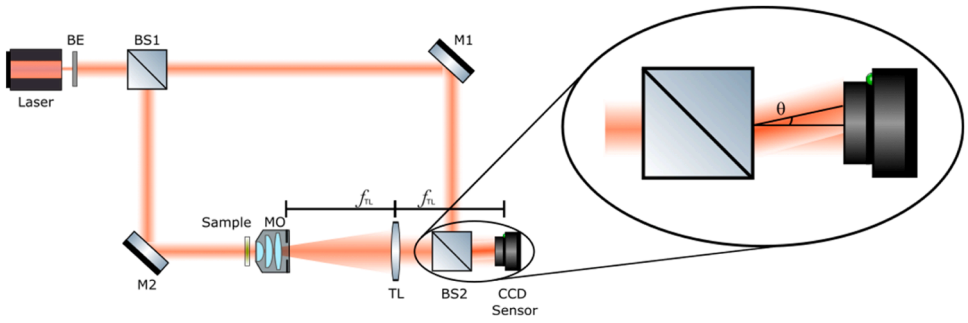

Fig. 1. Digital holographic microscope optical setup in telecentric configuration.

without phase distortions, regardless of the imaging sample and conditions.

Several algorithms have been reported in the literature for numerically reconstructing holograms with high precision. The first-generation DHM algorithms implement phase masks to counteract phase perturbations distorting the hologram. For example, Colomb et al. [16] proposed a polynomial fitting technique to generate a phase mask capable of compensating for the spherical wavefront introduced by the microscope objective and the tilting due to the off-axis configuration. However, this technique requires significant computational power. In the same year, Colomb et al. [17] proposed a method for implementing numerical lenses that could compensate for any phase aberration in the hologram. Seo et al. [18] also proposed a curve-fitting algorithm that required one hologram with a small amount of sample information in the field-of-view (FOV) to extract the curvature of the spherical wavefront, distorting the recorded hologram.

Phase-shifting-based techniques were originally proposed in the context of DHM to avoid the phase aberration compensation task while providing a computationally less intensive solution [19]. Atlan et al. [20] proposed a phase-shifting DHM technique in which four holograms with changes in phase and frequencies are required. Although phase shifting is quite robust for reconstructing holograms, it requires at least two holograms [21], challenging its application to real-time imaging. One of the first works to achieve phase compensation efficiently in a single shot was that proposed by Ferraro et al. [22] in 2003. In this work, the authors propose the comparison of three phase-compensation methods: in the first one, they use phase shifting to eliminate the twin image and the DC term of the hologram, and from the reconstruction, estimated using a simple parabolic adjustment, the curvature introduced by the imaging system. In the second proposed method, they calculate the curvature of the wavefront in the plane of the hologram (not in the reconstruction plane) and then, through propagation integrals, bring both holograms (hologram with sample and curvature correction hologram) to the same plane to make the subtraction of the phases. The third proposal uses a reference hologram, that is, a hologram without the sample's information but only information from the image-forming system. The three techniques were evaluated and compared in that study to determine which generated better phase maps. Although the third method requires the capture of two holograms, it is the one that generated the best results.

Although all the abovementioned methods can provide accurate phase measurements, they are based on iterative processes for calculating masks or require multiple recordings, restricting their use for high-speed quantitative phase imaging. In other words, these methods are unsuitable for evaluating dynamic phenomena like the movement of microorganisms or cellular processes *in vivo* [23]. Some proposal [24] suggests hybrid methods for phase compensation, where algorithms combine optical setups in a telecentric configuration with a brute-force search of the interfering angle to recover the sample's phase distribution with minimal distortions. While this proposal has a lower computational demand than previous methods [16,17] due to the physical compensation of the spherical phase factor with the telecentric configuration, it does not achieve high execution rates for phase compensation due to a brute-force search inside the algorithm. Heuristic algorithms have recently been proposed to alleviate the compensation algorithms' high computational complexity [25]. However, due to the probabilistic nature of these methods, the reconstructions may not always be as accurate as required in life science settings. Although several automated DHM reconstruction approaches [17,24,26–30] have been proposed, they often produce reconstructed phase images with phase nuisances, which hinder quantitative analysis. Moreover, the computational complexity of these methods still limits the proper recovery of phase maps free of aberration at fast rates, making quasi-real-time data processing a challenge [31]. Apart from these features, providing background phase stability is critical for dynamic sample analysis applications. However, the primary approaches mentioned earlier for obtaining accurate phase images in DHM do not validate this capability within hologram video sequences. In recent years, emerging proposals have employed learning-based models to address the phase aberration compensation problem [31–33]. These algorithms utilize neural network-based architectures to learn the effective compensation of off-axis DHM holograms from image pair datasets. While these statistical algorithms, once trained, can achieve full-field-of-view compensations in a fraction of a second, they necessitate substantial amounts of data during the training stage. As a result, there is still a gap in the literature concerning the proper implementation of an accurate deterministic method for processing holographic videos at reasonable processing times.

This paper proposes a solution to the challenges faced in reconstructing compensated phase map images from telecentric-based off-axis DHM holograms, in which phase maps are only distorted by a linear phase term due to the off-axis configuration. The proposed algorithm aims to quickly reconstruct phase maps with minimal changes in the background and high accuracy along the whole FOV. It utilizes an efficient semi-heuristic grid search method to estimate the carrier spatial frequency components within the +1-diffraction order in the power spectrum of the hologram. A modified version is also presented, which searches for compensating spatial frequencies between subsequent frames in a sub-pixel region to compensate for holographic videos. The method uses the accurate compensating spatial frequency components found in the first frame for the successive frames. The proposal is validated using three samples: a USAF test target, smearing red blood cells, and alive human sperm.

The structure of this paper is as follows: Section 2 outlines the experimental setup and describes the proposed methods, along with the validation metrics used for each algorithm. Section 3 presents the experimental results for static samples and holographic videos of dynamic human sperm and red blood cells with varying degrees of scattering. The proposed method's performance has been compared to traditional brute-force search [24] and heuristic [25] methods. Finally, in Section 4, the main findings of this research are summarized and concluded.

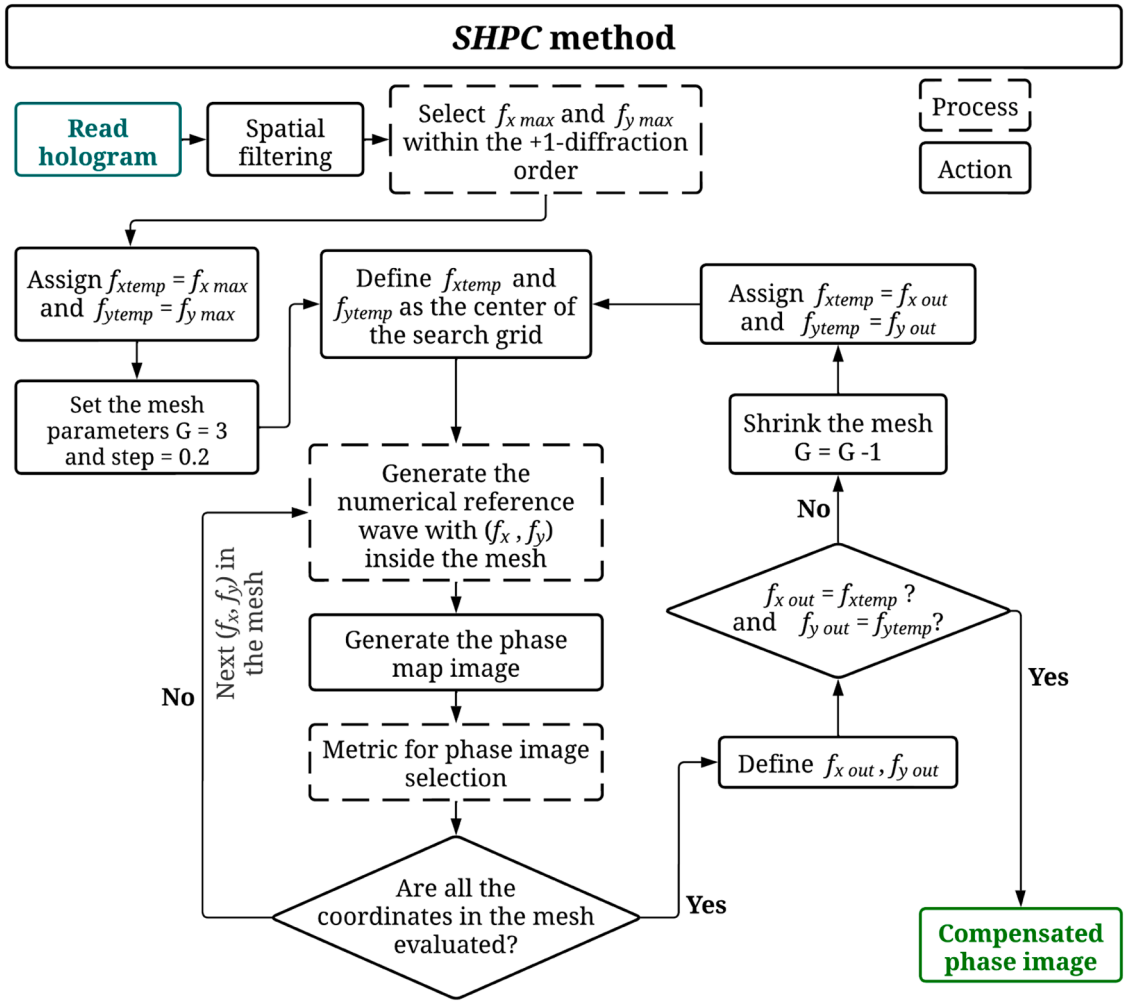

Fig. 2. Flowchart of the SHPC method.

2. Materials and methods

2.1. The optical setup

As previously mentioned, this research study uses a digital holographic microscope based on a Mach-Zehnder interferometer working on an off-axis configuration, as depicted in Fig. 1. A collimated plane beam emerging from a 633 nm He-Ne laser is divided into two light paths by the first beam splitter (BS1). The first path is the reference arm of the interferometer, in which a plane wave travels undisturbed until the first mirror (M1). M1 reflects the light towards the second beam splitter (BS2), which introduces a tilting angle between the object wavefront along the x- and y-axes. The second path is the object arm. In this path, the light travels until the second mirror (M2) and through the sample. Then, a 40x /0.65 NA infinity-corrected Microscope Objective (MO) lens and a Tube lens (TL) of focal length 200 mm are used to collect the light scattered by the sample. The MO and the TL lenses are set up in the telecentric configuration, forming a *4f-like* system, so the TL corrects the spherical wavefront distortion introduced by the MO lens [15]. Then, the object wavefront travels until the BS2, where it merges with the plane reference wave. The optical interference between the object and reference waves is recorded by a 1280×960 CCD sensor with square pixels of 3.75 μm^2, located at the back-focal plane of the TL. Since image-plane holograms are recorded, the reconstruction of these holograms does not require numerical propagation to focus the object information computationally. Nonetheless, we still need the spatial frequency filtering procedure and the phase compensation of the tilting interference angle to fully reconstruct accurate phase images, see Section 2.2.

With this optical setup, holograms have been recorded from three different samples: a commercial USAF test target since it is a calibrated sample and two biological samples, smearing of red blood cells (RBCs), and alive human sperm. Both biological samples were donated to this study by a local Colombian healthcare center. Static holograms have been recorded from the USAF target and the RBCs. In contrast, a holographic video is recorded from the human sperm sample to evaluate the potential of our proposed method in accurate quantitative phase imaging of holographic videos.

2.2. Proposed semi-heuristic phase compensation (SHPC) method

In DHM, the hologram distribution $h(x,y)$ recorded onto the digital sensor is:

$$h(x,y) = |o(x,y)|^2 + |r(x,y)|^2 + o^*(x,y)r(x,y) + o(x,y)r^*(x,y) \quad (1)$$

where (x,y) are the lateral spatial coordinates, and $|\ |^2$ and * denote the absolute modules square and conjugate operator, respectively. In Eq. (1), $o(x,y)$ is the complex amplitude distribution of the object wavefront, and $r(x,y)$ is the complex amplitude distribution of the reference plane wavefront. Since the DHM system works in an off-axis configuration, the different terms composing the hologram distribution Eq. (1)) are placed at different spatial frequencies on the hologram spectrum. In other words, the spectrum of the object and reference intensity

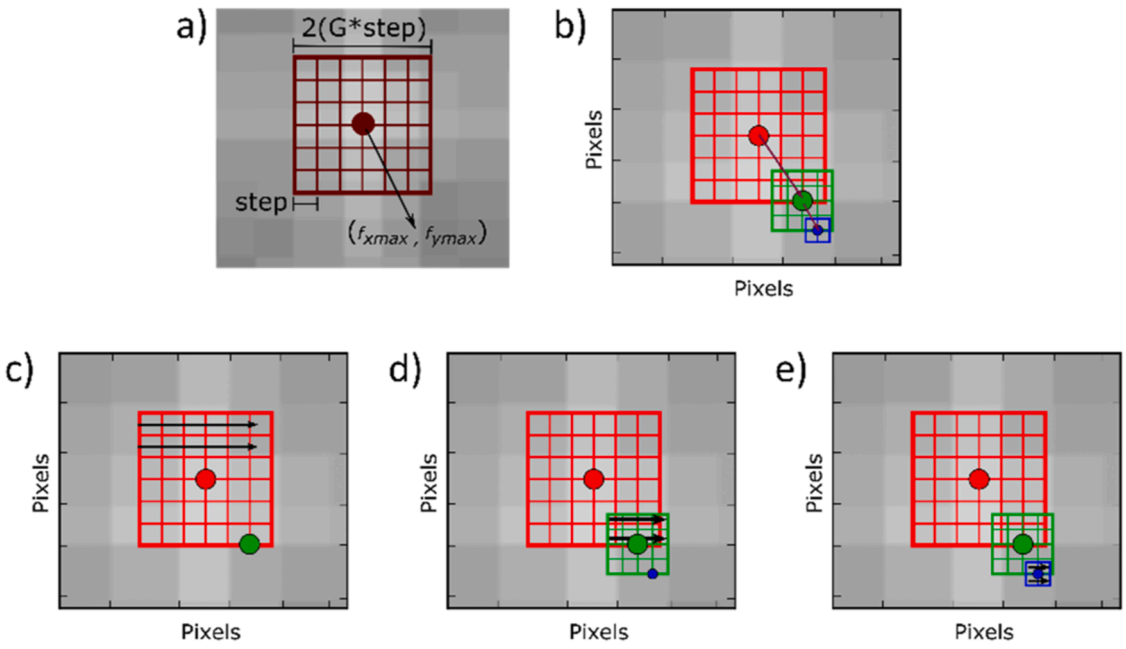

Fig. 3. Graphical description of the construction of the search grid inside the +1-diffraction term in the power spectrum of the recorded hologram for the SHPC proposal.

distributions are always placed at the frequency origin. However, the spectrum of the real image, FT$[o(x,y)r^*(x,y)]$, and virtual image, FT $[o^*(x,y)r(x,y)]$, are distributed symmetrically to the frequency's origin, and their position depends on the tilting angle between the object and reference waves. Then, numerically, one can apply a spatial filter in the hologram's spectrum to select the +1-diffraction order, i.e., Fourier transform of the real image $o(x,y)r^*(x,y)$. After filtering the spatial object frequencies from the hologram's spectrum, one applies the inverse Fourier transform to the filtered hologram and multiplies it with the digital replica of the reference wavefront. Since the physical reference wavefront is a linear phase ramp, the digital reference wavefront in each discrete lateral position can be numerically implemented as

$$r_D(m\Delta x, n\Delta y) = \exp\left[ik\left(m\Delta x\sin\theta_x + n\Delta y\sin\theta_y\right)\right]. \quad (2)$$

In Eq. (2), $k = 2\pi/\lambda$ is the wave number being λ the source's wavelength, (m,n) are the discrete lateral coordinates of the sensor, and $(\Delta x, \Delta y)$ are the pixel pitch in each dimension. The tilting angle $(\theta_x,\ \theta_y)$ in off-axis holograms can be estimated by the hologram size and the center position (i.e., maximum position) of the +1-diffraction term [25],

$$\theta_x = \sin^{-1}\left(\left(\frac{M}{2} - f_x\right)\frac{\lambda}{M\Delta x}\right)\ \theta_y = \sin^{-1}\left(\left(\frac{N}{2} - f_y\right)\frac{\lambda}{N\Delta y}\right), \quad (3)$$

where (M,N) are the hologram size in pixels along the horizontal and vertical direction, respectively, and (f_x,f_y) are the carrier spatial frequencies of the +1-diffraction term (i.e., the center position of the +1-diffraction term). A critical process in the compensation task in off-axis telecentric-based DHM is finding the accurate spatial frequency components (f_x,f_y) to avoid phase reconstructions with distortions [13]. Several algorithms have been proposed for this accurate spatial frequency determination, primarily based on brute-force approaches or heuristic searches. This study uses the brute-force *Full ROI* [24] and the heuristic telecentric universal DHM algorithm (*tuDHM*) [25] algorithms for comparison purposes. Both algorithms are publicly available within the *pyDHM* library [34].

The *Full ROI* algorithm, proposed by Trujillo et al. in 2016 [24], is a grid-search algorithm that generates a mesh around the brightest pixel of the +1-diffraction order and searches for the spatial frequencies that produce the best-compensated phase map. The mesh must be of several pixels with a small subpixel step to explore a large area and guarantee that the algorithm determines the exact frequency coordinates. This exhaustive search leads to a considerable computational complexity, which implies long processing times but guarantees well-compensated phase maps. In 2021, Castaneda et al. [25] proposed the heuristic-based *tuDHM* algorithm to alleviate the high computational complexity of the brute-force approach [24]. This method generates phase maps with minimum distortions while minimizing the algorithm's computational complexity. Unlike the grid-search process, the *tuDHM* algorithm minimizes a customized cost function that tracks the number of sawtooth fringes on the reconstructed phase images. However, the proposed cost function in Ref. [25] is non-convex, failing to produce fully compensated phase maps if the cost function finds a local minimum. Consequently, the performance of the *tuDHM* algorithm is unpredictable, lacking the required stability and accuracy for becoming the state-of-art phase reconstruction tool.

The proposed *Semi-heuristic Phase Compensation* (*SHPC*) method is an alternative approach to reconstructing phase maps with reduced processing time while avoiding the local-minimum problem. Fig. 2 shows the flowchart that summarizes the *SHPC* method.

This algorithm is a semi-heuristic method based on nested searches in which the grid size in every iteration is systematically reduced. First, the +1-diffraction term is identified, and then the brightest pixel within this term is located $(f_{x\ max},\ f_{y\ max})$, see Fig. 3a). The search mesh is implemented according to two parameters: G is a factor delimiting the search range as $(2*G*step)$, with the subpixel *step* size. In the first iteration, the parameter G is set to 3 and the *step* parameter to 0.2. These values have been selected after calibrating the algorithm with several DHM holograms containing different densities and scattering properties. The chosen values of G and *step* result in a mesh size of $9.38\times10^{-4}*\Delta x^{-1}$ in the horizontal direction and $12\times10^{-4}*\Delta y^{-1}$ in the vertical direction. Note that the mesh size differs along the horizontal and vertical directions since the hologram is not a square image, $M\neq N$. A phase image of each frequency coordinate pair within this mesh is generated by computing their corresponding complex conjugate reference wavefront (Eq. (2)) and multiplying it by the inverse Fourier transform of the spatially filtered hologram.

The best-compensated phase map within this mesh is then selected by choosing the phase distribution with the least number of phase

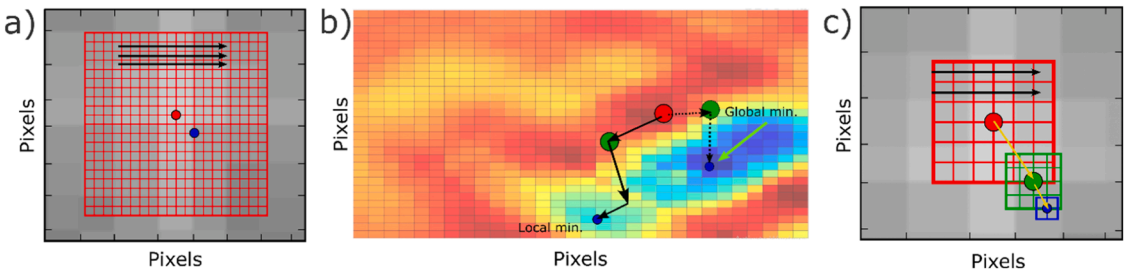

Fig. 4. Graphical description of the search for the spatial frequency components in each algorithm. (a) Grid search of the Full ROI algorithm, (b) Cost function minimization of tuDHM approach, and (c) Semi-heuristic grid search of SHPC method.

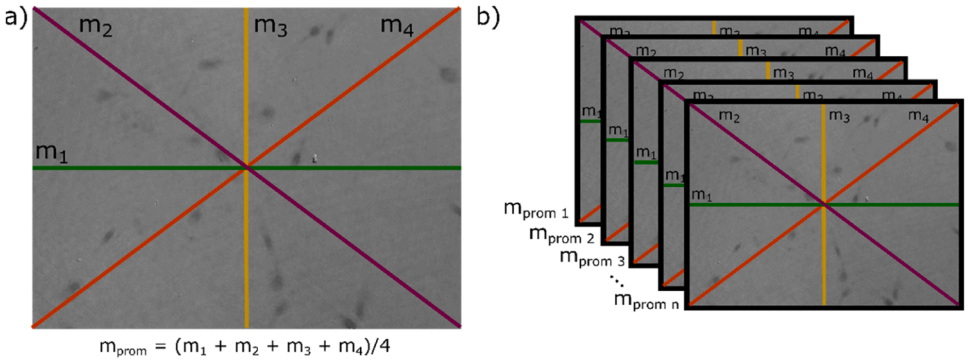

Fig. 5. Schematic representation of the background stability assessment: (a) illustration of the profile lines taken to compute the phase map slope, (b) illustration of the mean slope for each frame within the holographic video stack.

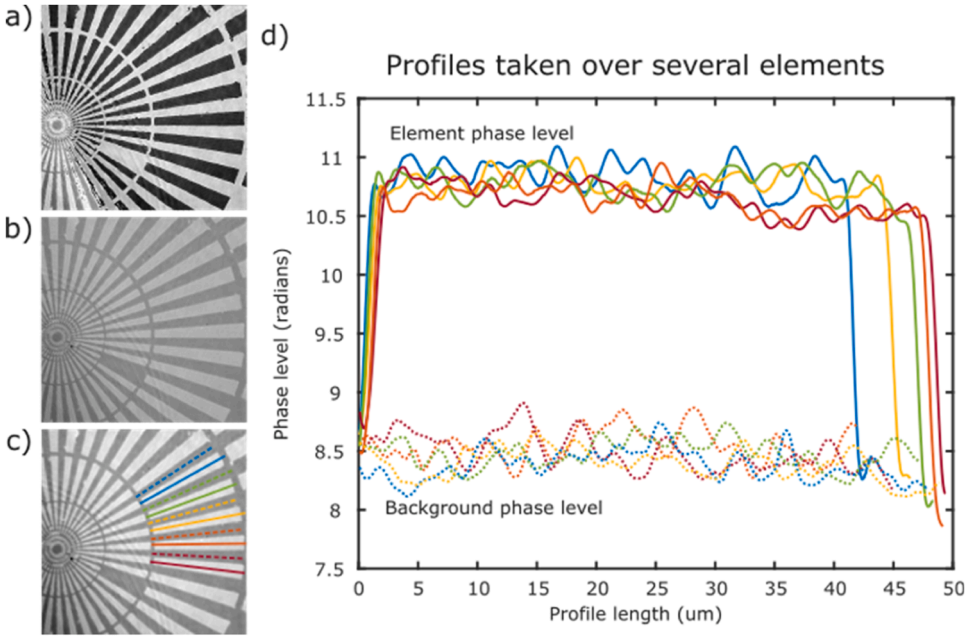

Fig. 6. Phase-accuracy validation of the ground truth method: (a) Wrapped reconstruction of the Full ROI, (b) Unwrapped reconstruction of the Full ROI, (c) Gaussian unwrapped reconstruction of the Full ROI, (d) Profiles of 6 elements and 5 sections of background.

jumps. In other words, the best-compensated phase map is found when its binarized map has the highest number of white pixels (white = 1 value). Therefore, one can automatically implement a maximum search for each phase map to estimate the best-compensated phase map, via Eq. (4).

$$\sum_{n}^{N}\sum_{m}^{M}\mathrm{Thresh}[\varphi_n(m,n),\ 0.1] = \mathrm{maxvalue}. \tag{4}$$

In Eq. (4), φ_n is the normalized phase map, (m,n) are integer numbers denoting the pixel position, (M,N) are the total number of pixels in the phase map, and Threash [■] represents the thresholding operation that converts any pixel value larger than 0.1 into one.

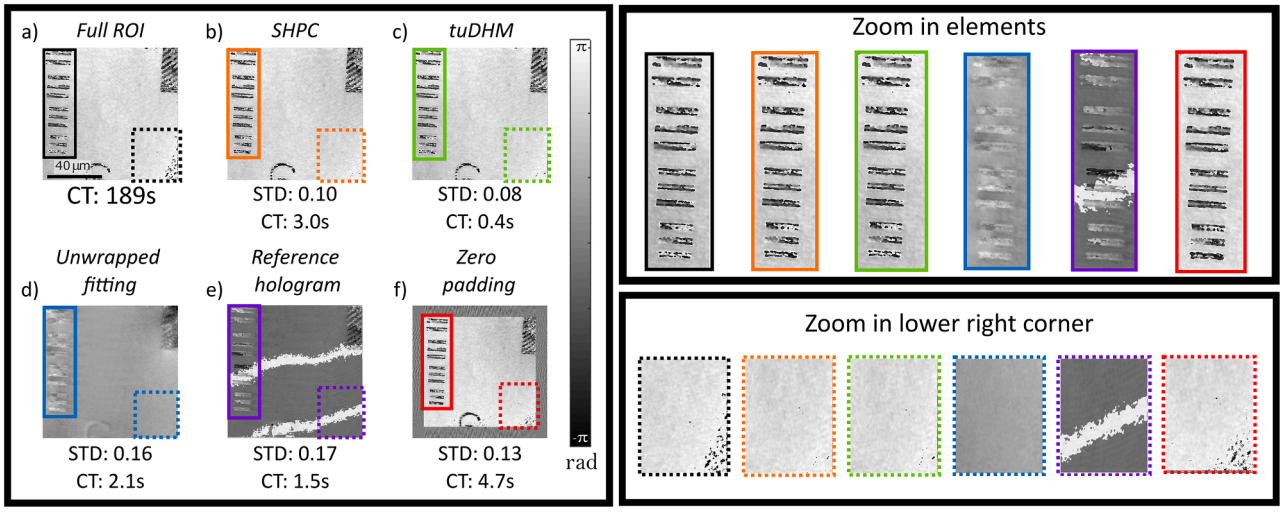

Fig. 7. Comparison of different reconstruction algorithms to remove the phase ramp due to the off-axis configuration: (a) Full ROI. (b) SHPC, (c) tuDHM, (d) unwrapped-fitting, (e) reference-hologram and (f) zero-padding algorithms. The STD value is also included in each phase map.

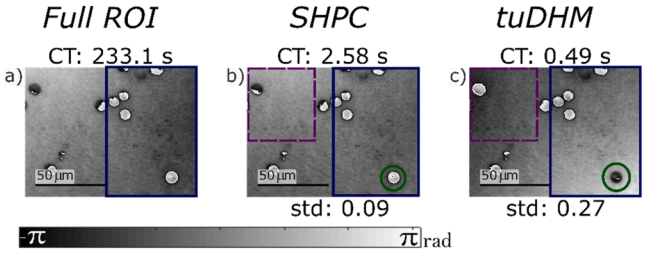

Fig. 8. Phase maps of single holograms compensated with the Full ROI (first column), the SHPC (second column), and the tuDHM (third column) for samples of RBC smearing (panel a–c), The compensation time (CT) to reach each compensated phase map is provided. The SHPC and tuDHM's phase maps standard deviations (std) with respect to the Full ROI phase map (ground-truth) are also reported.

This best-compensated phase map, obtained with the spatial frequency coordinates $(f_{x\ temp}, f_{y\ temp})$, serves as the starting point for the next search (Fig. 3c). A new mesh centered around the coordinates $(f_{x\ temp}, f_{y\ temp})$ is created with a reduced G value ($G = 2$), resulting in a smaller mesh size of $6.25 \times 10^{-4} * \Delta x^{-1}$ and $8 \times 10^{-4} * \Delta y^{-1}$ in the horizontal and vertical directions, respectively. The process is repeated until the values of the values of $(f_{x\ temp}, f_{y\ temp})$ coordinates converge. Successive meshes are created with a reduction of 1 in the parameter G (Fig. 3e). This process of shrinking the mesh is crucial to reduce the compensation times of the overall semi-heuristic search. Once the semi-heuristic nested search is done, the algorithm returns the best-compensated phase image and its corresponding carrier spatial frequency components. Supplemental material A provides an animated description of the proposed *SPHC* method.

Based on the descriptions of the *Full ROI, tuDHM*, and *SHPC* algorithms, it can be concluded that the primary difference between the three algorithms lies in the method used to search for the carrier spatial frequency components. It is important to highlight that each algorithm's search process is the most time-consuming step. Fig. 4 presents a graphical comparison of how each algorithm finds these spatial frequency values. Fig. 4a shows the extensive grid search of the *Full ROI* algorithm. The arrows indicate the directions in which the spatial frequencies within the grid are evaluated. In panel b), the complete heuristic behavior of the cost function minimization by the *tuDHM* method is observed. The red solid point represents the initial seed of the search, the green circles depict a partial step in the search process, and the blue circles represent the final spatial frequency components for

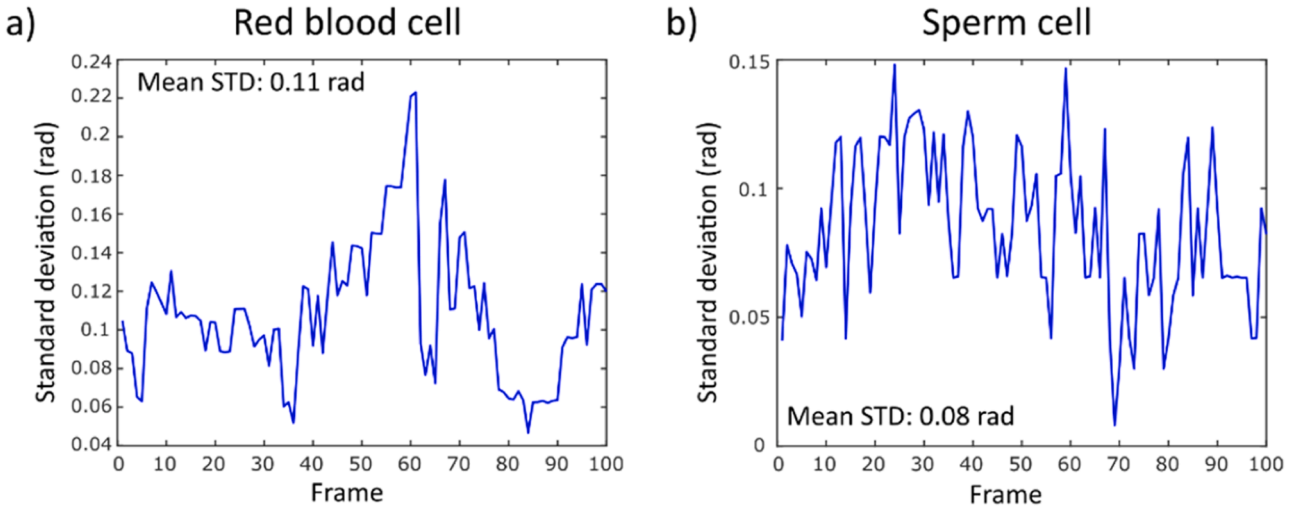

Fig. 9. Standard deviation per frame of the holographic video of (a) Red blood cells and (b) sperm cells.

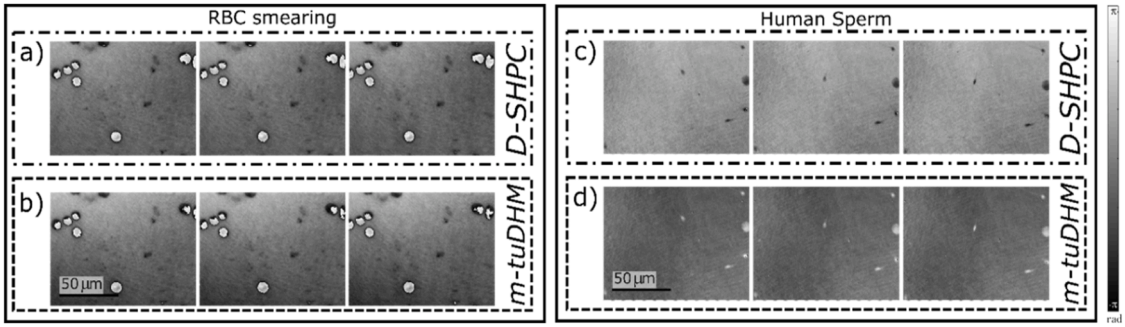

Fig. 10. Frames of the two holographic videos: (a) and (b) unsaturated RBC compensated with the D-SHPC and the m-tuDHM, and (c) and (d) Human sperm compensated with the D-SHPC and the m-tuDHM.

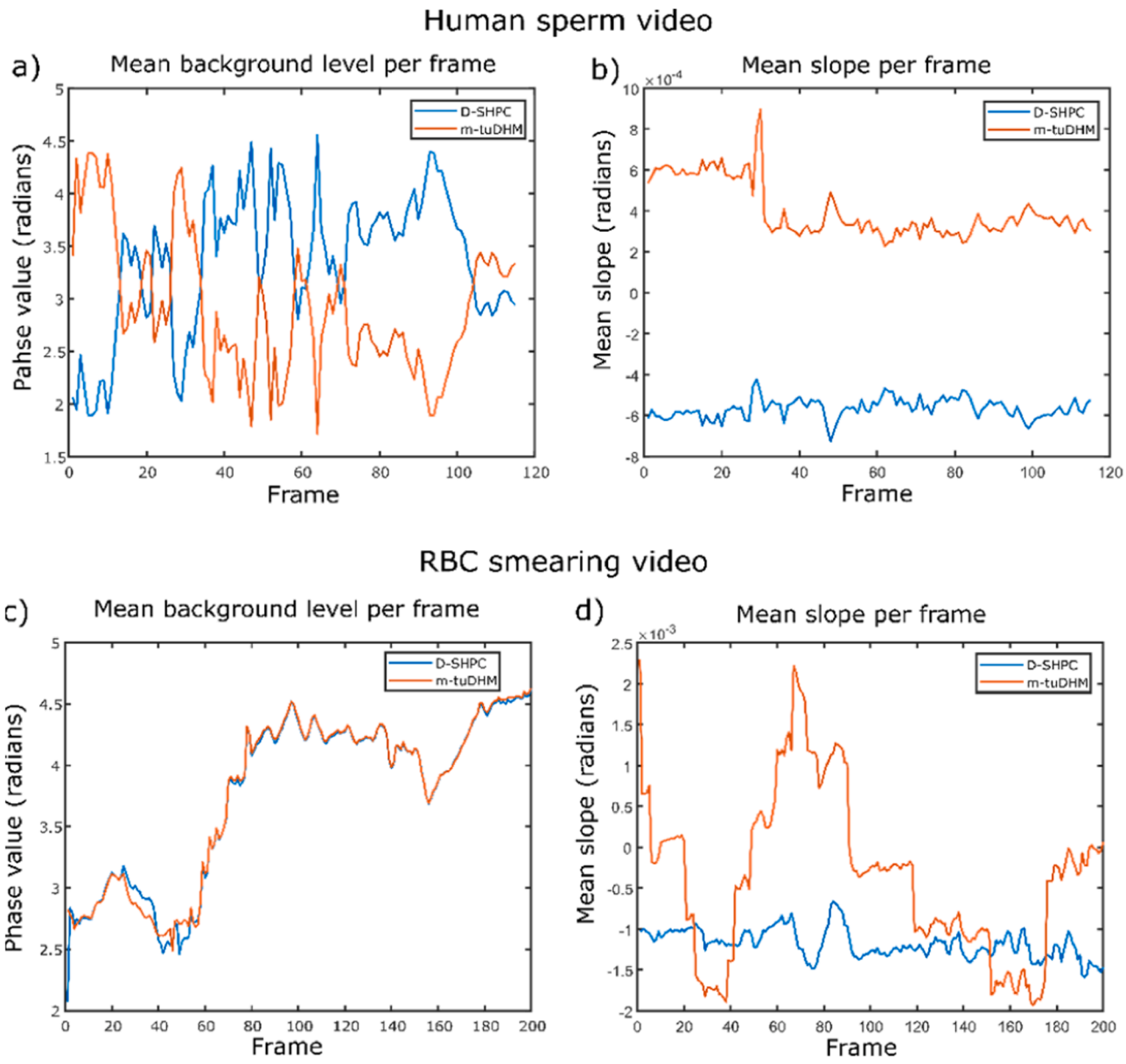

Fig. 11. Mean background phase level and mean phase slope for each frame in holographic videos of fresh human sperm [panel (a) and (b)] and Red Blood Cells [panel (c) and (d)] samples.

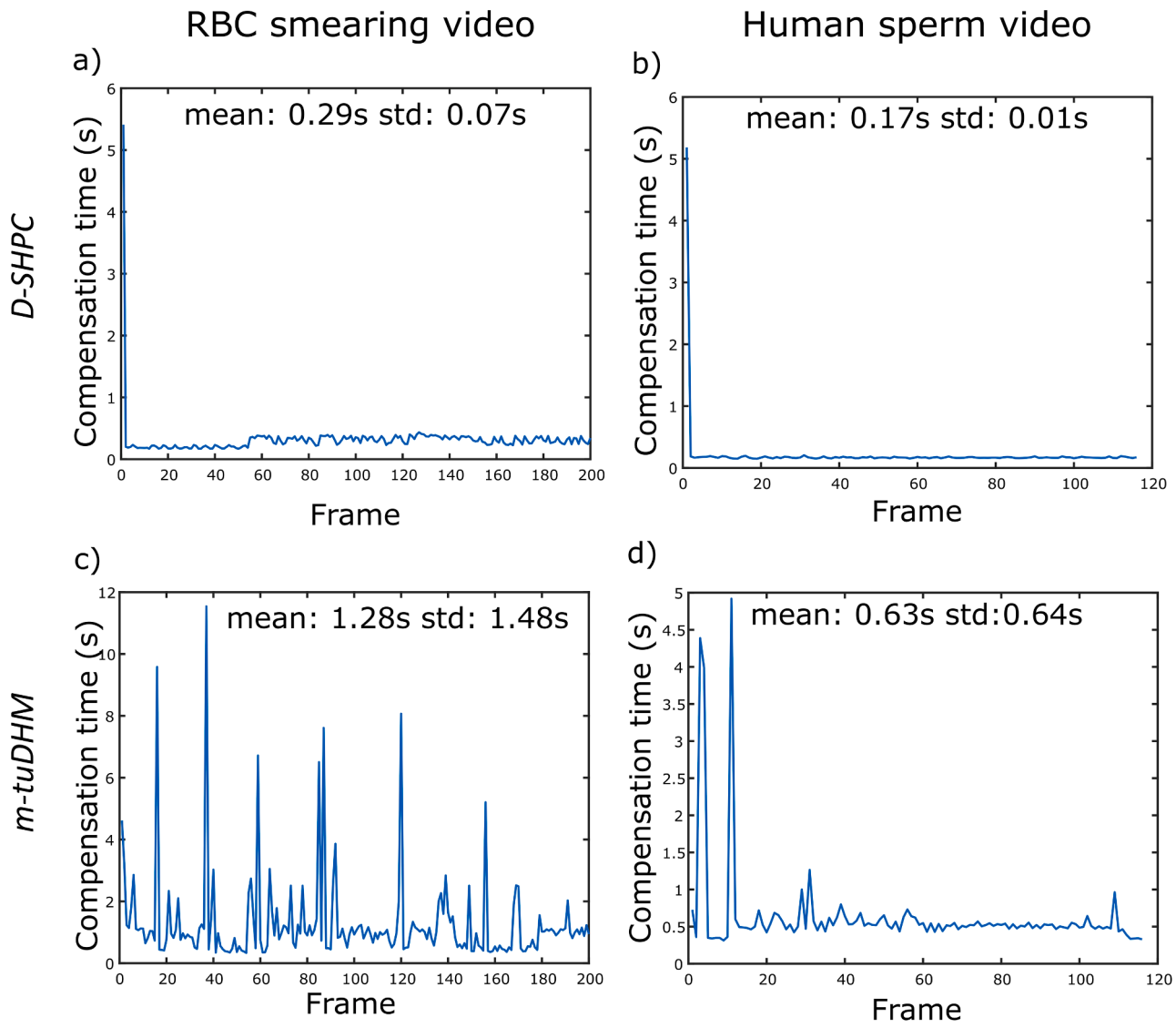

Fig. 12. Compensation times of the smearing RBC video frames (a) and c) and the human sperm video frames (b) and d)) when compensated with the D-SHPC and the m-tuDHM.

compensation. The solid arrows illustrate a path that leads to a local minimum, and the dashed arrow illustrates the path that leads to the global minimum. This schematic demonstrates that this heuristic search does not always reach the global minimum value marked with the light green arrow. As a result, not all images are correctly compensated. Finally, in panel c), one can observe the size reduction of the grid during the search process of the *SHPC*. The red point is the central point of the first grid (i.e., $f_{x\ max}$, $f_{y\ max}$), the green one depicts a partial step in the search process ($f_{x\ temp}$, $f_{y\ temp}$), and the blue one represents the coordinates of the best-compensated phase map ($f_{x\ out}$, $f_{y\ out}$). The black arrows show the evaluation direction of the grid, while the orange arrows illustrate the path of the selected compensation coordinates.

2.3. Dynamic SHPC: specimen variations in holographic videos

Studying living organisms' behavior and evolution is crucial in many biological applications. To do this, it is often necessary to reconstruct phase images quickly and accurately from a stack of holograms with minimum background level changes. A modification of the proposed *SHPC* algorithm, *Dynamic SHPC (D-SHPC)*, is proposed to address the challenge of dynamic phase reconstructions. The *D-SHPC* method is also based on nested searches and is specifically designed to provide reconstructed phase images from holographic videos. In the first frame of the video, the *SHPC* method is applied to find the spatial frequency components that compensate for the hologram accurately ($f_{x\ out}$, $f_{y\ out}$). For subsequent frames, ($f_{x\ out}$, $f_{y\ out}$) values are in the upper right corner of a new search grid that is significantly smaller in size. This reduction can be made because, within subsequent holograms of the same video stack, the locations of the compensating spatial frequency components do not vary in a range greater than $11.25 \times 10^{-4} \Delta x^{-1}$ (i.e., less than 1 pixel away from each other). As a result, for the second video frame, G is set to 0.2 and the *step* to 0.1, and in subsequent iterations for the remaining frames, G is reduced by a value of 0.1. The process continues as described in Section 2.2 but with new values of G and *step* for the search grid. Reducing the first search grid size (i.e., $G = 0.2$ in *D-SHPC* instead of $G = 3$ as in the *SHPC*) is crucial for further reducing the processing time. With these modifications, *D-SHPC* generates compensated phase maps at rates that allow for studying dynamic phenomena, such as the movement of human sperm.

2.4. Comparisons with previously-reported DHM methods

Several comparisons are proposed to validate the overall performance of the *SHPC* and the *D-SHPC*. First, the *Full ROI* phase maps are

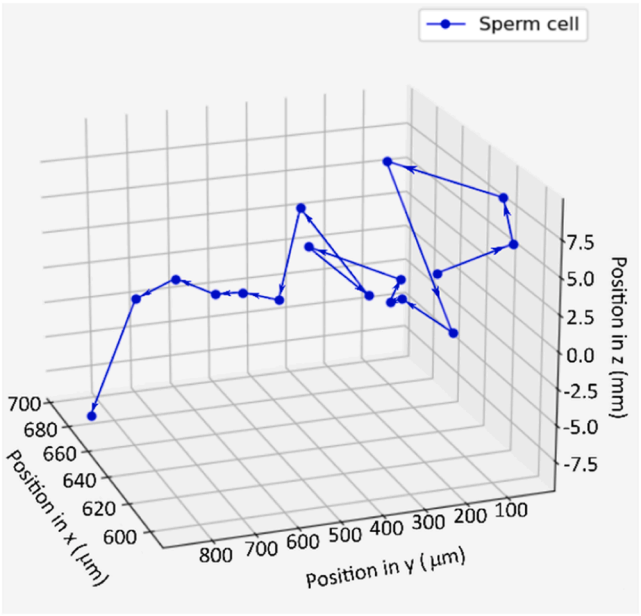

Fig. 13. Trajectory of sperm cell.

used as a ground-truth element for the static version of the algorithm. Therefore, the *SHPC, tuDHM*, and three additional methods are compared against the *Full ROI* approach. The first approach, derived from interferometric inverse synthetic aperture radar imaging, applies zero-padding to the recorded hologram, aiming to increase the frequency sampling and provide more accuracy to estimate the parameters of the digital reference wave [35]. The second method uses an unwrapped-fitting approach in which the phase distribution is reconstructed by computing the angle of the inverse Fourier Transform of the filtered hologram spectrum. Since we have not performed any phase compensation, the reconstructed phase distribution presents the phase ramp due to the off-axis configuration. After the reconstructed phase map is unwrapped, we perform a least squares surface fitting of the unwrapped phase map to estimate the parameters of the overall phase ramp, generating a digital phase ramp matrix [30]. Finally, both phase maps (i.e., the reconstructed phase map with the phase ramp and the digital phase ramp) are subtracted from one another to obtain a compensated phase map with the sample's information. The third method consists of subtracting a reference hologram (i..e., hologram without object distribution) from the recorded hologram of the sample [22].

For evaluating the *D-SHPC* performance, a modified version of the *tuDHM* algorithm has also been implemented for comparison purposes; see Section 3 for more details.

2.5. Evaluation metrics

Two metrics (i.e., processing time and reconstruction accuracy) are selected to quantify essential performance parameters of the *SHPC* algorithm against the *Full ROI, tuDHM, zero-padding, unwrapped-fittig,* and *reference- hologram* methods. The processing time is determined by the execution time of the phase compensation process (i.e., compensation time, CT) in each algorithm, excluding image loading, visualization, and other steps common to all methods. The similarity of the compensations against the ground truth method is evaluated using an image similarity metric [36]. The *Full ROI* image is the ground truth for the phase map images. The standard deviation of the phase maps, Eq. (5), is measured to evaluate this parameter.

$$\sigma_{\varphi} = \sqrt{\left\langle \left(\Delta\varphi_o - \Delta\varphi_s\right)^2 \right\rangle + \left\langle \left(\Delta\varphi_o - \Delta\varphi_s\right) \right\rangle^2}. \quad (5)$$

In Eq. (6), σ_{φ} represents the standard deviation of the phase error, $\Delta\varphi_o$ is the *Full ROI* phase image and $\Delta\varphi_s$ is the phase map generated by the other five methods (see Section 2.4), and $\langle\blacksquare\rangle$ is the mean operator.

When evaluating the dynamic samples, the goal is to determine the stability of the background in holographic video compensation. To achieve this, the slope of profile lines in each phase map's horizontal (m_1), vertical (m_3), and principal diagonal directions (m_2, m_4) are calculated, as illustrated in Fig. 5a. Each image's average slope (m_{prom}) is then calculated, and the variation of this value throughout the holographic video stack is analyzed for each algorithm (Fig. 5b). Additionally, each image's average background level is determined through a segmentation process in which only the background information is extracted and used to calculate an average value. The segmentation process is done by applying a strong Gaussian Filter to the reconstructed phase image (i.e., kernel size = 7), discriminating the background information from the object one. From the segmented phase map, the image's mean value is calculated as the background mean level in a single frame, enabling us to study how the background level changes throughout subsequent reconstructions.

3. Results

Before presenting the experimental results, the validity of the *Full ROI* as the ground truth method must be established by analyzing the reconstructed phase image of a hologram of a commercial Star Target from the Benchmark Technologies Quantitative Phase Target. Fig. 6(a) and (b) shows the wrapped and unwrapped reconstructed phase images provided by the *Full ROI* method. After applying a Gaussian filter to the unwrapped reconstruction to eliminate phase noise inside each element [Fig. 6 (c)], 10 profiles of the star target (e.g., 5 across the star element and 5 across the background) have been plotted in Fig. 6 (d). The phase difference between the background and the star element is equal to 10.66 ± 0.1 radians. Assuming that the difference in refractive index from the optical glass and the air is 0.52, the corresponding thickness of the star element is 353.41 ± 6.37 nm. Since there is an error of 0.98 % between the reconstructed thickness and the expected value (e.g., 350 nm), one can confirm the accuracy of the Full ROI algorithm for phase reconstructions and its validity for being the ground truth method in this work.

The first experiment compares the phase map recovered by the *SHPC* algorithm and those from the *Full ROI* (ground-truth), *tuDHM, zero-padding, unwrapped-fitting, and reference-hologram* methods. These computational algorithms were executed in a computer station hosting an Intel(R) Xenon(R) running at 3.60 GHz. The results of this experiment are shown in Fig. 7.

The standard deviation (STD) of each algorithm against the *Full ROI* is reported in the bottom part of each image. Also, the compensation time (i.e., CT) is reported for each method. From this information, one can observe that the *tuDHM* and the SHPC provide the lowest STD values. On the other hand, the *unwrapped-fitting* and the *reference-hologram* methods are the ones with the highest STD values, providing the worst reconstructed phase maps (see, zoom in elements, in Fig. 7) eventhough the background in those phasemaps are the most homogeneous (see zoom in lower right corner). This is evident when visually analyzing the quality of the resulting phase maps in Fig. 7(d) and (e). Although the reconstructed phase map obtained by the *zero-padding* method is similar to the one provided by the *SHPC* one, their quantitative values differ (i.e., the STD value is 0.10 rad for the *SHPC* method and 0.13 rad for the *zero-padding* one). In addition, the *zero-padding* method requires more time when performing the compensation. The performance of the *unwrapped-fitting* method is significantly dependent on the performance of the unwrapping algorithm, not necessarily leading to good phase maps. The unwrapping algorithm used in this study was proposed by Xia & Picart et al. in 2006 [37,38]. Because the unwrapping algorithms are based on probabilities, this algorithm tend to fail in some regions of the estimated unwrapped phase map when

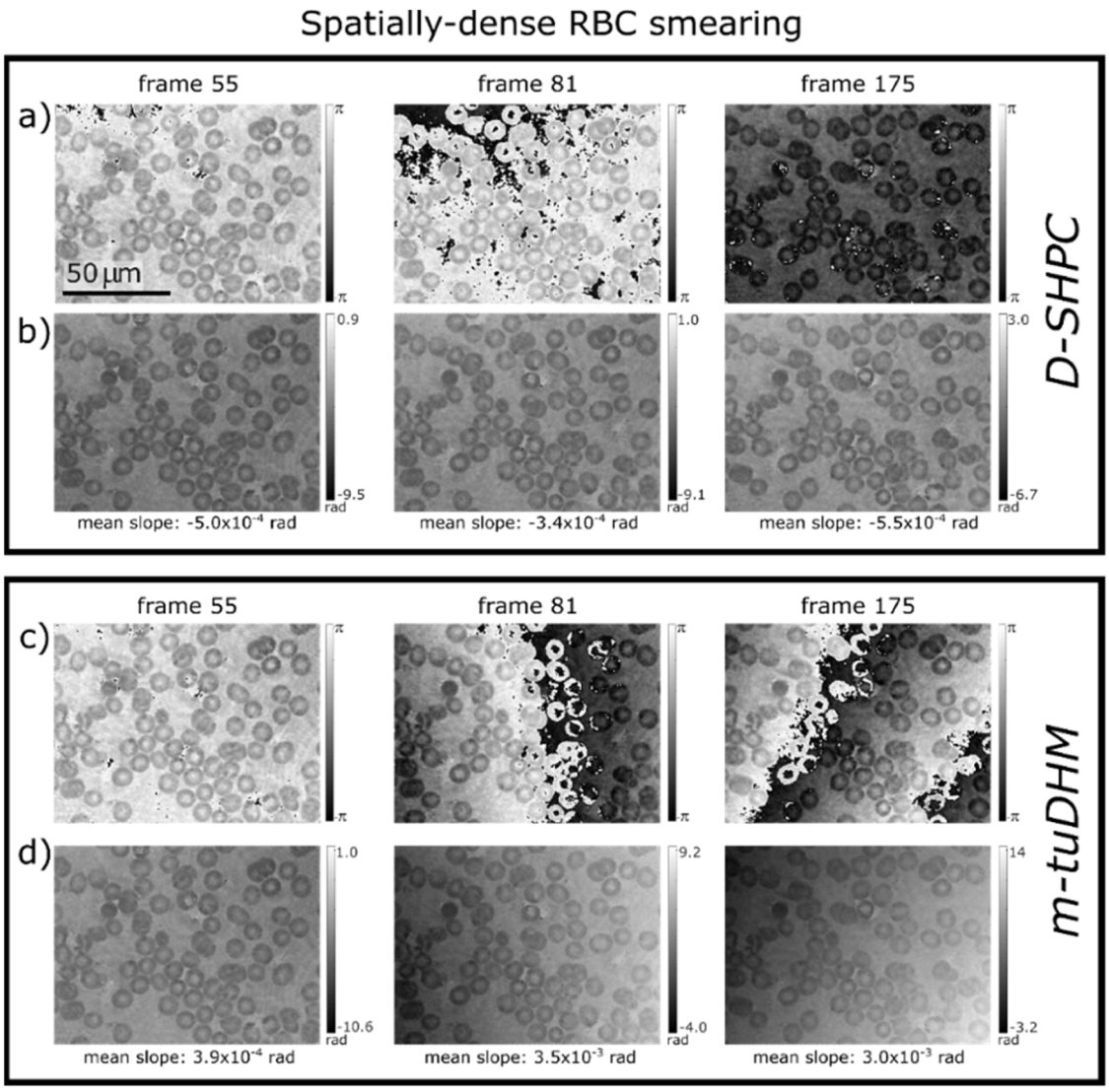

Fig. 14. Reconstructed phase images of three different frames of the holographic video for a spatially dense RBC smearing when compensated with the D-SHPC (panel a) and the m-tuDHM (panel c) and their correspondence unwrapped phase map (panel b and d, respectively).

objects producing several phase jumps. Regarding the reference hologram algorithm, we see that it has a qualitative and quantitative performance similar to that of unwrapped-fitting, with a shorter processing time.

The *tuDHM* and *SHPC* models are considered for the next experiment since they have the best reconstructed phase maps (i.e., lowest STD values). In Fig. 8, we present the compensation time (CT) and the standard deviation (std) to the ground-truth phase image. The *SHPC* is around 92 times faster than the *Full ROI* method for all samples according to the compensation times. Additionally, while the *tuDHM* method has a shorter execution time than the *SHPC* method, its accuracy is lower in this biological sample, as evidenced by the purple rectangles in panels b) and c) and their *std* values. Within these areas, the *tuDHM* phase map displays a remaining uncompensated phase ramp, represented as a darker gray level within the purple rectangle. This phase ramp in the *tuDHM* image results in the RBC within the green circle appearing wrapped in the image and displaying a different phase value from the other RBCs in the same frame and a different value from the same cell in the *Full ROI* and the *SHPC* compensations.

When comparing the region in the blue rectangle in panels b) and c) to panel a), one can observe that the reconstruction of the *SHPC* is more similar to the ground-truth phase map than the *tuDHM* reconstruction since the latter presents a remaining tilting in the left bottom corner, represented with the transition of the background level from gray to white. The error supports this result reported for each image, where it is observed that the metric is an order of magnitude lower in the case of *SHPC* (0.09 radians) than in the *tuDHM* (0.27 radians).

The third experiment evaluates the *D-SHPC* algorithm's capability to accurately reconstruct holographic videos from dynamic phenomena. The first validation involves calculating the standard deviation of each phase map reconstructed by *D-SHPC* against those reconstructed with the *Full ROI* (ground truth). For this validation, Eq. (5) is computed for 100 frames of each sample (red blood cells and sperm cells). Fig. 9 presents the calculated STD per frame and the average value for each sample. The results obtained for each video are in agreement with the static results of the *SHPC* (see Figs. 7 and 8). Therefore, the reconstructed phase maps of the holographic videos by the proposed method are guaranteed to be compensated similarly to those reconstructed with the ground truth method.

A modified version of the *tuDHM* algorithm (*m-tuDHM*) has been implemented for fairness in the comparison. The *m-tuDHM* method utilizes the compensation spatial frequency coordinates of frame *n-1* as the seed for the minimization process in frame *n*. This ensures that both algorithms initiate their compensation process around the carrier

frequencies of the previous frame. The experimental validation of these methods involved recording samples of fresh human sperm and smearing red blood cells. Fig. 10 displays several phase images reconstructed from holographic videos by the *D-SHPC* and *m-tuDHM* methods. Panels a) and b) show three frames from the RBC sample, while panels c) and d) are the phase reconstructions for the human sperm holographic video. Overall, all the phase images are well compensated. However, there is a noticeable difference in the reconstructed background level between the *D-SHPC* and *m-tuDHM* methods for the phase images shown in panels c) and d). This discrepancy highlights the presence of a constant offset in the phase background levels introduced by the m-tuDHM method, as previously discussed. The supplemental materials are the reconstructed phase videos for both samples and algorithms. The compensated reconstructed videos are also available in the supplemental material: S1 video for RBC_DRF_14sep.mp4 (*D-SHPC*-yielded video), S2 video for RBC_tuDHM_14sep.mp4 (*m-tuDHM*-yielded video), S6 video for sperm_DRF.mp4 (*D-SHPC*-yielded video) and S7 sperm_tuDHM.mp4 (*m-tuDHM* -yielded video).

The mean background phase level and the mean phase slope in each video frame are measured as described in Section 2.4. Fig. 11 presents these results for each sample. In Fig. 11a, one observes that the mean background phase levels of the compensated phase images by the *m-tuDHM* method are complementary to the values obtained by the *D-SHPC* method around π radians, meaning they are each other's negatives in phase. In contrast, Fig. 11c shows that the mean phase value in each reconstruction frame behaves similarly for both methods. However, when analyzing the mean phase slope of each frame in the holographic videos presented in panels b) and d) of Fig. 11, it can be seen that the *D-SHPC* produces more stable compensations than the *m-tuDHM*. In both panels, the mean phase slopes of the *D-SHPC* images have less variability than those of the *m-tuDHM* images as denoted by their standard deviations: 4.85×10^{-5} radians (*D-SHPC*) and 1.36×10^{-4} radians (*m-tuDHM*) in panel b), and 1.75×10^{-4} radians (*D-SHPC*) and 9.99×10^{-4} radians (*m-tuDHM*) in panel d). The high variability in the mean slope value of the *m-tuDHM* reconstructions is due to the heuristic nature of the algorithm since the optimization process can follow different paths in each frame. Therefore, the final reconstruction can present a high variance from the previous one.

To further compare the *D-SHPC* and *m-tuDHM* performances, the compensation times of each algorithm for each holographic video are also reported, see Fig. 12. A clear difference between the algorithms is distinguishable. The reconstruction times of the *m-tuDHM* are random, as is expected for heuristic algorithms, while the *D-SHPC* processing times remain constant. The first compensation in the *D-SHPC* method takes around 5 s due to the larger searching grid of the first frame; however, the remaining frames are compensated in less than 0.3 s.

The compensation times of the *D-SHPC* are fast enough to provide compensated phase images at a rate that allows for studying some dynamic processes, which makes this proposal suitable for living tracking applications, among others. To validate this assumption, a fragment of the holographic video of the sperm sample has been extracted to perform a single-cell XYZ tracking. The video is available in S3 supplemental material (video_sperm_Tracking.mp4). The selected specimen is localized easily in all video frames due to the stability of the phase background provided by the *D-SHPC* algorithm. Fig. 13 presents the 4D trajectory (XYZ + time) of one single cell for illustration. Each point is computed in that figure with a time interval of 50 ms.

A spatially dense sample of moving red blood cells has been recorded as a final experiment to evaluate the algorithm's capability. In Fig. 14, some frames of the video are displayed. The compensated reconstructed videos are also available in the supplemental material: S4 video for RBC_DRF_27sep.mp4 (*D-SHPC*-yielded video) and S5 video for RBC_tuDHM_27sep.mp4 (*m-tuDHM*-yielded video). In these reconstructed videos, some frames present noisy artifacts in the resulting phase maps; see frames 81 and 175 from the video sequences in Fig. 14. The reconstructed phase images in Fig. 14 have different background reference, resulting in relative phase values of the specimens that differed from those of previous frames in the sequence. Nonetheless, the *D-SHPC* algorithm still generates the best-compensated phase image among the tested methods since the absolute measured phase difference of each specimen is still correctly recovered. This can be observed in the second and third column of panel a) and c) in Fig. 13, where the unwrapped [39] phase map of the *D-SHPC and m-tuDHM* image are presented. While the unwrapped phase map of the *m-tuDHM* (second and third column of panel c) presents a phase ramp along the horizontal and diagonal axis, the *D-SHPC* reconstruction is a plane phase map. To support this statement, the mean slope of the image was also calculated and reported under each frame. These results reassure *D-SHPC's* capability to reconstruct spatially dense samples correctly.

4. Conclusions

This work presents a semi-heuristic algorithm (*SHPC*) to reconstruct phase images with minimum distortion in the full field-of-view (i.e., 1280×960 pixels or 4.8 × 3.6 cm^2). The method is aimed at holograms recorded by an off-axis Digital Holographic Microscope (DHM) set at telecentric mode, providing high background stability and overall accuracy. The studied samples are a USAF test target, two smeared red blood cell samples, and an alive human sperm sample. The accuracy of phase compensation methods in off-axis DHM depends on correctly determining the spatial frequency coordinates of the center of the +1-diffraction term in the Fourier spectrum of the holograms to build a precise digital reference compensating wave. After thoroughly comparing with previously reported numerical phase compensation methods, this research has chosen the algorithm referenced in [20] as the ground-truth method to validate the results, ultimately yielding the best outcomes. This method proposes a brute-force grid search around the brightest pixel of the +1-diffraction order, combined with a slight searching step to ensure finding the best-compensated phase map at the expense of a high computational cost. Under the same conditions, *SHPC* recovers phase images with a maximum of 0.12 radians of standard deviation (std) compared to those obtained with the ground-truth method, but around 92 times faster. The *SHPC* method differs from the traditional method of searching a large grid with a minimum step. Instead, it performs several sequential searches in smaller areas in the Fourier domain of each hologram. Following a guided search path, the method performs these searches around each iteration's partial best-compensating spatial frequency components. By using this approach, processing times are reduced while still ensuring accurate reconstructions in each run. A comparison was also made to assess *SHPC* with the fully heuristic *tuDHM* approach [25]. The comparison results showed that although *SHPC* required more processing time, it consistently produced accurate phase reconstructions for all the tested samples, in contrast to *tuDHM*, which generated inaccurate reconstructions for some samples.

A modified version of *SHPC*, called *Dynamic SHPC* (D-SHPC), has been developed to accurately retrieve phase maps from sequences of holograms. The modified version's most time-consuming step is compensating the holographic sequence's first frame. However, it has been observed that the compensating spatial frequency components of subsequent frames in a holographic video locate within a radius of less than $11.25 \times 10^{-4} \Delta x^{-1}$ in their Fourier spectrum. As a result, the compensation process for the first frame can be treated differently from the rest of the holograms. Once the algorithm identifies the compensation frequencies for the first frame, repeating the comprehensive search in subsequent frames is unnecessary. This reduction in the grid search enables fast execution while preserving the method's accuracy. When tested on a computer station powered by an Intel(R) Xenon(R) running at 3.60 GHz, the *D-SHPC* renders at a maximum of six (5.88 ∼ 6) frames per second (i.e., 0.17 $s \pm 0.01$ s) in reconstructing phase maps from 1280×960 pixel holograms. The *D-SHPC* has been tested with a

holographic video of an alive human sperm sample, obtaining almost plane reconstruction (mean slope of $-\ 1.2\times\ 10^{-3}\ \pm\ 7.75\times\ 10^{-4}$ radians in each phase map) in less than 0.2 s. The proposed method's performance was compared with a modified version of the *tuDHM* approach for holographic video processing. The results show that *D-SHPC* outperforms the fully heuristic method, producing more accurate phase results and ensuring greater background stability between successive frames of the tested videos, even for highly scattering samples.

All the performed tests show that the *SHPC* algorithm is highly suitable for particle tracking applications since it can quickly generate phase maps with minimum background changes. The reconstructed sequence provided by the *D-SHPC* algorithm has been used to track an individual sperm cell, validating the assumption successfully.

One primary drawback of the proposed method, as with other phase compensation methods in DHM, is that the compensation time depends on the dimensions and complexity of the hologram, such as the cell density in the sample. A parallelized algorithm version will be implemented to decrease compensation times in future studies. Specifically, the generation of numerical references will be parallelized to reduce the compensation process time. Despite these potential limitations, the application of *SHPC* and its modified version *D-SHPC* enables the use of DHM in various fields, where precise and consistent phase reconstructions can be achieved within a reasonable processing time.

Funding

This study was partially funded by internal research projects at Universidad EAFIT, provided by the Vicerrectoría de Ciencia, Tecnología e Innovación. A. Doblas acknowledges the support provided by National Science Foundation (NSF) through her NSF CAREER grant (grant number 2042563).

CRediT authorship contribution statement

Sofía Obando-Vásquez: Conceptualization, Methodology, Software, Validation, Formal analysis, Investigation, Data curation, Writing – original draft, Visualization. **Ana Doblas:** Conceptualization, Methodology, Validation, Formal analysis, Resources, Writing – review & editing, Supervision, Funding acquisition. **Carlos Trujillo:** Conceptualization, Methodology, Validation, Formal analysis, Resources, Writing – review & editing, Supervision, Project administration, Funding acquisition.

Declaration of Competing Interest

The authors declare that they have no known competing financial interests or personal relationships that could have appeared to influence the work reported in this paper.

Data availability

Codes: https://sobandov.github.io/SHPC/. Images and videos https://drive.google.com/drive/folders/1WyeEGHmJ1Rf9Y2XSYC516ykqV5rXEAzI?usp=share_link.

Acknowledgments

S. Obando-Vaquez and C. Trujillo acknowledge the support provided by Vicerrectoría de Ciencia, Tecnología e Innovación from Universidad EAFIT. A. Doblas acknowledges the support from the University of Memphis, the Herff College of Engineering, and UMass Dartmouth.

Supplementary materials

Supplementary material associated with this article can be found, in the online version, at doi:10.1016/j.optlaseng.2023.107937.

References

[1] Kemper B, Langehanenberg P, Kosmeier S, Schlichthaber F, Remmersmann C, von Bally G, et al. Digital holographic microscopy: quantitative phase imaging and applications in live cell analysis. Handbook of coherent-domain optical methods. 1–2. Springer; 2013. p. 215. https://link.springer.com/referenceworkentry/10.1007/978-1-4614-5176-1_6.

[2] Kim MK. Digital holographic microscopy. Digital holographic microscopy: principles, techniques, and applications. New York: Springer; 2011. p. 149–90. M. K. Kim, ed.

[3] G. Coppola, S. De Nicola, P. Ferraro, A. Finizio, S. Grilli, al Giuseppe Coppola, M. Iodice, C. Magro, and G. Pierattini, (2003). Characterization of MEMS structures by microscopic digital holography. 4945(25), 71–78, 10.1117/12.471989.

[4] Y. Emery, E. Solanas, N. Aspert, A. Michalska, J. Parent, and E. Cuche, (2013). MEMS and MOEMS resonant frequencies analysis by Digital Holography Microscopy (DHM). 8614, 56–61, 10.1117/12.2009221.

[5] B. Kemper, D.D. Carl, J. Schnekenburger, I. Bredebusch, M. Schäfer, W. Domschke, and G. von Bally, (2006). Investigation of living pancreas tumor cells by digital holographic microscopy. 11(3), 034005, 10.1117/1.2204609.

[6] H. Sun, B. Song, H. Dong, B. Reid, M.A. Player, J. Watson, and M. Zhao, (2008) Visualization of fast-moving cells *in vivo* using digital holographic video microscopy. 13(1), 014007, 10.1117/1.2841050.

[7] Warnasooriya N, Joud F, Bun P, Tessier G, Coppey-Moisan M, Desbiolles P, Atlan M, Abboud M, Gross M. Imaging gold nanoparticles in living cell environments using heterodyne digital holographic microscopy. Opt Express 2010;18(4):3264–73.

[8] Pavillon N, Kühn J, Moratal C, Jourdain P, Depeursinge C, Magistretti PJ, Marquet P. Early cell death detection with digital holographic microscopy. PLoS ONE 2012;7(1):e30912.

[9] B. Kemper, A. Bauwens, A. Vollmer, S. Ketelhut, P. Langehanenberg, J. Muthing, H. Karch, and G. von Bally, (2010). Label-free quantitative cell division monitoring of endothelial cells by digital holographic microscopy. 15(3), 036009, 10.1117/1.3431712.

[10] Anand A, Chhaniwal VK, Javidi B. Real-time digital holographic microscopy for phase contrast 3D imaging of dynamic phenomena. J Disp Technol 2010;6(10):500–5. **6**(10), 500–505.

[11] Rappaz B, Marquet P, Cuche E, Emery Y, Depeursinge C, Magistretti PJ. Measurement of the integral refractive index and dynamic cell morphometry of living cells with digital holographic microscopy. Opt Express 2005;13(23):9361–73. **13**(23), 9361–9373.

[12] Takeda M, Ina H, Kobayashi S. Fourier-transform method of fringe-pattern analysis for computer-based topography and interferometry. J Opt Soc Am 1982;72(1):156–60.

[13] Cuche E, Marquet P, Depeursinge C. Spatial filtering for zero-order and twin-image elimination in digital off-axis holography. Appl Opt 2000;39(23):4070–5.

[14] Sánchez-Ortiga E, Doblas A, Saavedra G, Martínez-Corral M, Garcia-Sucerquia J. Off-axis digital holographic microscopy: practical design parameters for operating at diffraction limit. Appl Opt 2014;53(10):2058–66. **53**(10), 2058–2066.

[15] A.I. Doblas, E. Sánchez-Ortiga, M. Martínez-Corral, G. Saavedra, and J. Garcia-Sucerquia, (2014). Accurate single-shot quantitative phase imaging of biological specimens with telecentric digital holographic microscopy. 19(4), 046022, 10.1117/1.JBO.19.4.046022.

[16] Colomb T, Cuche E, Charrière F, Kühn J, Aspert N, Montfort F, Marquet P, Depeursinge C. Automatic procedure for aberration compensation in digital holographic microscopy and applications to specimen shape compensation. Appl Opt 2006;45(5):851–63. **45**(5), 851–863.

[17] Colomb T, Montfort F, Kühn J, Aspert N, Cuche E, Marian A, Charrière F, Bourquin S, Marquet P, Depeursinge C. Numerical parametric lens for shifting, magnification, and complete aberration compensation in digital holographic microscopy. J Opt Soc Am A 2006;23(12):3177–90.

[18] Seo KW, Choi YS, Seo ES, Lee SJ. Aberration compensation for objective phase curvature in phase holographic microscopy. Opt Lett 2012;37(23):4976–8. **37**(23), 4976–4978.

[19] Mico V, Zalevsky Z, García J. Common-path phase-shifting digital holographic microscopy: a way to quantitative phase imaging and superresolution. Opt Commun 2008;281(17):4273–81.

[20] Atlan M, Gross M, Absil E. Accurate phase-shifting digital interferometry. Opt Lett 2007;32(11):1456–8.

[21] Castañeda R, Buitrago-Duque C, Garcia-Sucerquia J, Doblas A. Fast-iterative blind phase-shifting digital holographic microscopy using two images. Appl Opt 2020;59(24):7469–76.

[22] Ferraro P, De Nicola S, Finizio A, Coppola G, Grilli S, Magro C, Pierattini G. Compensation of the inherent wave front curvature in digital holographic coherent microscopy for quantitative phase-contrast imaging. Appl Opt 2003;42(11):1938–46.

[23] Kemper B, von Bally G. Digital holographic microscopy for live cell applications and technical inspection. Appl Opt 2008;47(4):A52–61. Vol. 47, Issue 4, pp. A52-A61.

[24] Trujillo C, Castañeda R, Piedrahita-Quintero P, Garcia-Sucerquia J. Automatic full compensation of quantitative phase imaging in off-axis digital holographic microscopy. Appl Opt 2016;55(36):10299–306. **55**(36), 10299–10306.
[25] Castaneda R, Doblas A. Fast-iterative automatic reconstruction method for quantitative phaseimage with reduced phase perturbations in off-axis digital holographicmicroscopy. Appl Opt 2021;60(32):10214–20.
[26] He X, Nguyen CV, Pratap M, Zheng Y, Wang Y, Nisbet DR, Williams RJ, Rug M, Maier AG, Lee WM. Automated Fourier space region-recognition filtering for off-axis digital holographic microscopy. Biomed Opt Express 2016;7(8):3111–23.
[27] Xin L, Xiao W, Cao R, Wu X, Ferraro P, Pan F. Automatic compensation of phase aberration in digital holographic microscopy with deep neural networks for monitoring the morphological response of bone cells under fluid shear stress. In: Proceedings of the SPIE. 11786; 2021. 117860O.
[28] Obando-Vásquez S, Trujillo C. Computationally efficient phase aberration compensation method for digital holographic microscopy of biological samples. Computationally efficient phase aberration compensation method for digital holographic microscopy of biological samples. Optical Society of America; 2021. C. Boudoux, K. Maitland, C. Hendon, M. Wojtkowski, K. Quinn, M. Schanne-Klein, N. Durr, D. Elson, F. Cichos, L. Oddershede, V. Emiliani, O. Maragò, S. Nic Chormaic, N. Pégard, S. Gibbs, S. Vinogradov, M. Niedre, K. Samkoe, A. Devor, D. Peterka, P. Blinder, and E. Buckley, eds. (OSA Technical Digest2021.
[29] Liu S, Lian Q, Qing Y, Xu Z. Automatic phase aberration compensation for digital holographic microscopy based on phase variation minimization. Opt Lett 2018;43(8):1870–3.
[30] Di J, Zhao J, Sun W, Jiang H, Yan X. Phase aberration compensation of digital holographic microscopy based on least squares surface fitting. Opt Commun 2009;282(19):3873–7.
[31] Castaneda R, Trujillo C, Doblas A. Video-rate quantitative phase imaging using a digital holographic microscope and a generative adversarial network. Sensors 2021;21(23):8021.
[32] Li Z, Wang F, Jin P, Zhang H, Feng B, Guo R. Accurate phase aberration compensation with convolutional neural network PACUnet3+ in digital holographic microscopy. Opt Lasers Eng 2023;171:107829.
[33] Chang T, Ryu D, Jo Y, Choi G, Min HS, Park Y. Calibration-free quantitative phase imaging using data-driven aberration modeling. Opt Express 2020;28(23):34835–47.
[34] Castañeda R, Trujillo C, Doblas A. pyDHM: a Python library for applications in digital holographic microscopy. PLoS ONE 2022;17(10):e0275818.
[35] Yuan Z, Wang J, Zhao L, Gao M, Zhang Y. A phase compensation method for azimuth interpolation based on zero-padded DFT in interferometric ISAR imaging. In: Proceedings of the CIE international conference on radar (RADAR); 2016. p. 1–5.
[36] Montresor S, Picart P. Quantitative appraisal for noise reduction in digital holographic phase imaging. Opt Express 2016;24(13):14322–43. **24**(13), 14322–14343.
[37] Xia H, Montresor S, Guo R, Li J, Yan F, Cheng H, Picart P. Phase calibration unwrapping algorithm for phase data corrupted by strong decorrelation speckle noise. Opt Express 2016;24(25):28713–30.
[38] Xia HT, Guo RX, Fan ZB, Cheng HM, Yang BC. Non-invasive mechanical measurement for transparent objects by digital holographic interferometry based on iterative least-squares phase unwrapping. Exp Mech 2012;52(4):439–45.
[39] Ghiglia DC, Pritt MD. Two-dimensional phase unwrapping: theory, algorithms, and software. J Investig Dermatol 1998;120(1):520.